Chapter 2

Circular hydraulic jump

2.1 Description of the phenomenon

When a jet of fluid hits a surface, the fluid spreads out radially along the surface. At a certain distance from the jet one notices a sudden thickening of the flow called the hydraulic jump. The hydraulic jump forms a ring of a certain radius with the jet at its center. If this experiment were performed in a kitchen sink, the hydraulic jump would generally be non-stationary, and the circular form of the jump could be distorted. In the laboratory, however, one can achieve a perfectly stationary radially-symmetric flow. The setup of the experiment is shown in figure 2.1. The experiment was performed by C. Ellegaard, A. E. Hansen and A. Haaning. A photograph of a stationary and radially-symmetric hydraulic jump, obtained in the experiment, is shown on figure 2.2. A stationary jet hits the center of a smooth radial plate and the fluid runs off the rim. The circular plate is submerged into the fluid. The depth, measured relative to the top of the rim, is denoted in figure 2.1

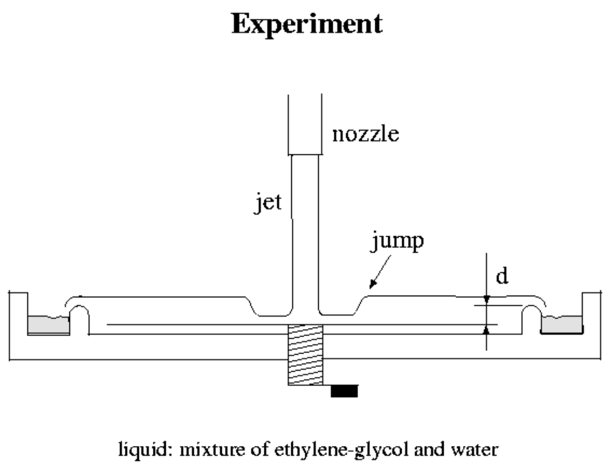

Figure 2.1: Setup of the hydraulic jump experiment.

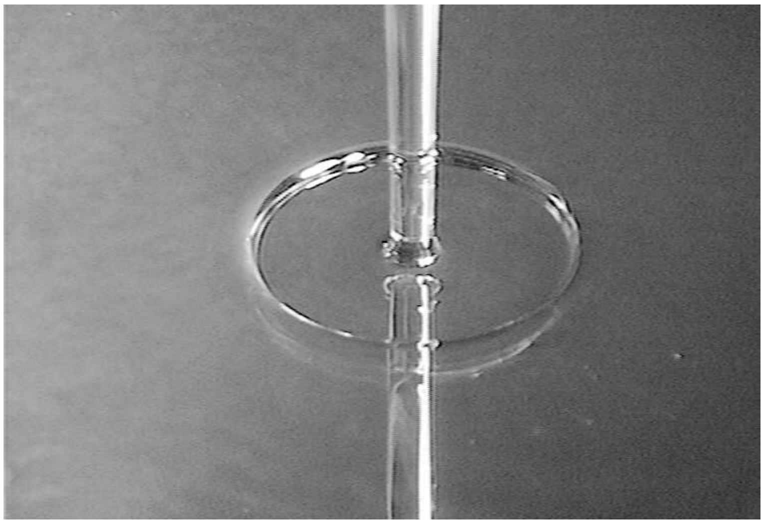

Figure 2.2: The circular hydraulic jump, courtesy of A. E. Hansen and A. Haaning.

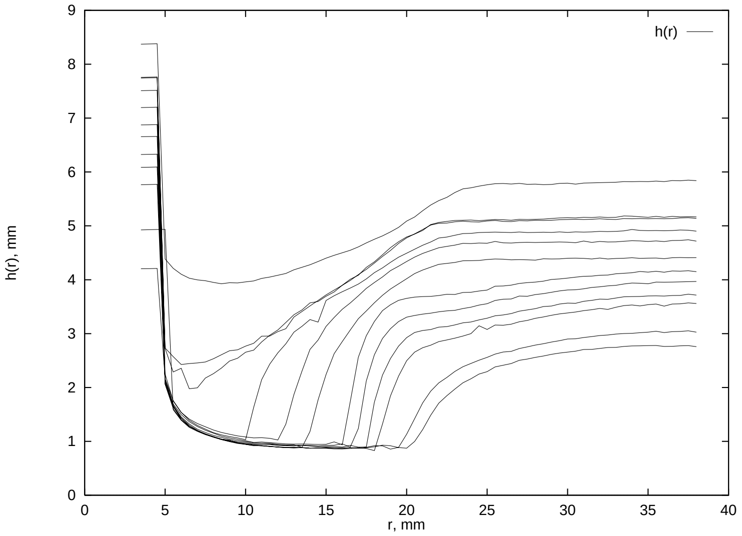

Figure 2.3: Height profiles $h(r)$ for different values of the external height h_{ext}. The height $h(r)$ approaches h_{ext} for large values of r.

as d. The height of the fluid layer is measured with respect to the plate. For a large radius the height h_{ext} is controlled by the depth d, as is illustrated on figure 2.1. Usually, h_{ext} exceeds d by $1-2$ millimetres. The depth d (and thus the external height h_{ext}) can be changed in the experiment: a motor moves the plate in the vertical direction. The motor is shown as a manual handle in figure 2.1. We vary h_{ext} and observe the corresponding change in the structure of the flow. The height profiles for different values of the external height h_{ext} are presented in figure 2.3. Theoretical explanation of experimental results in figure 2.3 will be the goal of this chapter.

It has been known for a long time [1, 2] that the jump contains a separation eddy whose inner edge determines the position of the jump, as is illustrated in figure 2.4(a). We shall call such a hydraulic jump *a jump of 'type 1'*. When the external height h_{ext}

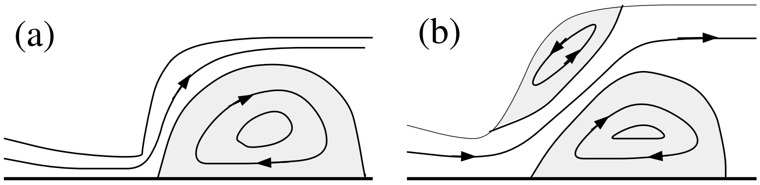

Figure 2.4: A schematic picture showing the transition from a) type 1 flow (an eddy on the bottom) to b) type 2 flow (an eddy on the bottom and a roller on the top).

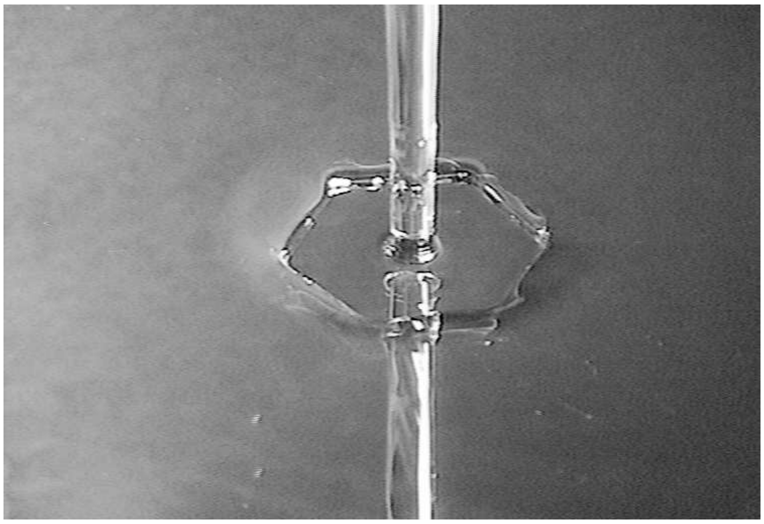

Figure 2.5: A regular polygon with 6 corners, courtesy by A. E. Hansen and A. Haaning.

is increased beyond some critical value, a *wave-breaking bifurcation* is observed. For low external height h_{ext}, the flow only has an eddy on the bottom, as shown in figure 2.4(a). If the external height h_{ext} is large enough, the flow has both an eddy on the bottom and a 'roller' on the top, as shown on figure 2.4(b). Such a flow shall be called *a jump of 'type 2'*. The transition from a type 1 to a type 2 flow is reminiscent of the breaking of a wave, therefore we use the name *wave-breaking bifurcation* for describing this transition. The flow of 'type 2' is also stationary and radially-symmetric. For a flow of type 2, the height around the jump increases much more slowly than for type 1. This can be readily observed on figure 2.3. If the external height is increased even further, breaking of the radial symmetry occurs. The hydraulic jump ceases to be circular, and takes the form of regular polygons. The polygons sometimes rotate around the jet, and the rotation can occur in both directions. The number of corners in the polygons usually decreases as the external height increases. However, the number of corners of the polygons can also occasionally increase when the external height increases [4]. We present a photograph of a polygon with 6 corners in figure 2.5.

The phenomenon of the circular hydraulic jump has attracted considerable attention in the literature. Usually, this problem was considered using the boundary layer approach. Kurihara [3] and Tani [1] had attempted to describe this phenomenon including gravity effects and considering a self-similar profile for the velocity. Watson [5] neglected gravity effects, which allowed him to derive exact solutions of the boundary layer equations. The jump was realized as a Rayleigh shock (see below), connecting 'inner' and 'outer' solutions.

The inconsistency of Watson's solutions was pointed out in [6], where gravity was taken into account. There, we calculated approximate solutions and introduced rescaling of the equations. The hydraulic jump was still realized as a shock. Thus, the structure of the jump (as illustrated on figure 2.4) remained largely unexplained. To describe the structure of the jump, one has to deal with the separation of boundary layer (the eddy inside the jump region). We have seen in the previous chapter that the integral methods allow a description of flows exhibiting the separation of a boundary layer. Thus, we shall apply these integral methods to flows with a free surface. Our models will be relatively simple, but quite accurate in describing the structure of the jump.

We shall mention that only the flow of type 1 can be described by our models. We can neither describe a flow of type 2 nor determine the transition point from type 1 to type 2. In the end of the chapter, we shall mention a possible way of describing flows of type 2 and predicting the wave-breaking bifurcation. In addition, two possible methods for solving this problem (albeit applied to the problem of channel flow) are described in chapter 5. The breaking of the radial symmetry and the formation of polygons will not be discussed at all: at present, we do not have any theoretical understanding of this problem.

2.1.1 Shocks and conservation laws

Before we go into details of our model, we review Lord Rayleigh's theory of shock conditions (conservation laws) for river bores. Similar shock conditions are usually applied to the problem of the circular hydraulic jump [5, 6], as we have already mentioned. The hydraulic jump or a river bore is treated as a shock (discontinuity in the flow). Across such a shock, the mass and momentum flux must be conserved [5]. We shall work in the coordinate system where the position of the jump does not change. The circular hydraulic jump is stationary, so we work just in the laboratory frame of reference. For river bores, we choose a system of coordinates moving together with the bore. Conservation of mass flux across the jump is given by

$$v_1 h_1 = v_2 h_2, \tag{2.1}$$

and conservation of momentum flux across the jump is

$$h_1(v_1^2 + gh_1/2) = h_2(v_2^2 + gh_2/2). \tag{2.2}$$

Here h is the height, v is the average velocity and the index $1, 2$ corresponds to the values before and after the jump, respectively. In this case, the energy flux is dissipated with the rate [5]

$$Q_{e2} - Q_{e1} = -\frac{gQ}{8\pi}\frac{(h_2 - h_1)^3}{h_1 h_2} < 0. \tag{2.3}$$

The dissipation is attributed to the turbulent motions and waves carrying energy. In the circular hydraulic jump, however, another dissipation mechanisms must be sought, since experimentally we observe that the flow is perfectly stationary. It is reasonable therefore to attribute the dissipation of energy to laminar viscous forces. This leads to the question: why can't the momentum be dissipated by laminar viscous friction at the plate? Our models allow us to check to what extent Lord Rayleigh's conservation laws (2.1-2.2) are valid for the stationary hydraulic jump.

2.2 Derivation of the model

2.2.1 Governing equations

Throughout this chapter, we assume the flow to be stationary and radially symmetric, and neglect surface tension effects.

The Navier-Stokes equations (1.1) for a radial, incompressible, stationary flow are [8]:

$$\begin{aligned} uu_r + wu_z &= -p_r/\rho + \nu u_{zz} + \nu \Delta_r u \\ uw_r + ww_z &= -p_z/\rho + \nu w_{zz} + \nu \Delta'_r w - g \end{aligned} \tag{2.4}$$

where u is the radial component of the velocity, w is the vertical component of the velocity, ν is the viscosity and p is the pressure. The subscripts r and z denote the partial derivatives with respect to r and z, respectively, and the linear operators Δ_r and Δ'_r are

$$\begin{aligned} \Delta_r u &= u_{rr} + u_r/r - u/r^2 \\ \Delta'_r w &= w_{rr} + w_r/r. \end{aligned} \tag{2.5}$$

The incompressibility condition (continuity equation) is

$$u_r + u/r + w_z = 0. \tag{2.6}$$

The boundary condition on the bottom of the plate is the no-slip condition:

$$u = w = 0 \qquad \text{on } z = 0. \tag{2.7}$$

On the free surface $z = h(r)$ we apply the kinetic and the dynamic boundary conditions. The kinetic condition means that a particle starting at the surface at some r_0 will remain at the surface for all r:

$$w = uh' \qquad \text{on } z = h(r). \tag{2.8}$$

Here, the prime denotes the derivative with respect to r. For the incompressible stationary flow, (2.8) is equivalent to conservation of the mass flux Q:

$$r \int_0^h u \mathrm{d}z = Q/2\pi \equiv q. \tag{2.9}$$

The dynamic boundary conditions describe the balance of forces normal and tangential to the surface. For the normal component, the normal stress balances the external pressure:

$$p/\rho = 2\nu w_z - \nu h'(u_z + w_r) \qquad \text{on } z = h(r). \tag{2.10}$$

The second dynamic boundary condition arises from the fact that the tangential stress has to vanish:

$$0 = 2\nu h'(u_r - w_z) - \nu(1 - h'^2)(u_z + w_r) \qquad \text{on } z = h(r). \tag{2.11}$$

As we have mentioned, surface tension effects were neglected in (2.10) and (2.11).

The system of equations (2.4) and the boundary conditions (2.10)-(2.11) are too complicated to analyse. We shall try to simplify the system by keeping only the terms essential in the boundary layer approximation. We shall thus start with the justification of the boundary layer approximation for this problem.

2.2.2 Boundary layer approximation

One can observe experimentally that the thickness of fluid in the hydraulic jump experiment is very small, especially in the inner part of the jump. The typical scales for the radial velocity u_*, vertical velocity w_*, radius r_* and thickness of the fluid z_* were derived in [6] using the parameters $q = Q/(2\pi)$, ν and g entering (2.4) and (2.9) as

$$\begin{aligned} u_* &= q^{1/8}\nu^{1/8}g^{3/8} \\ w_* &= q^{-1/4}\nu^{3/4}g^{1/4} \\ r_* &= q^{5/8}\nu^{-3/8}g^{-1/8} \\ z_* &= q^{1/4}\nu^{1/4}g^{-1/4}. \end{aligned} \tag{2.12}$$

A typical set of parameters used in the experiments are $\nu \simeq 0.1$ cm^2/s (mixture of ethylene-glycol and water) and $Q \simeq 30$ cm^3/s, (thus $q = Q/(2\pi) \simeq 5$ cm^3/s). The numerical values of the characteristic scales are thus

$$\begin{aligned} u_* &\simeq 12 \text{ cm/s} \\ w_* &\simeq 0.7 \text{ cm/s} \\ r_* &\simeq 3 \text{ cm} \\ z_* &\simeq 0.15 \text{ cm}. \end{aligned} \tag{2.13}$$

We see that the typical vertical scale z_* is much smaller than the typical radial scale r_*. Thus, the typical variation in the z direction is much faster than the variation in the r direction, i.e.,

$$\frac{\partial}{\partial z} \gg \frac{\partial}{\partial r}. \tag{2.14}$$

Correspondingly, the typical radial velocity scale u_* is much larger than the vertical velocity w_*:

$$w(r,z) \ll u(r,z). \tag{2.15}$$

Observe that (2.14)-(2.15) are precisely the boundary layer approximations given by (1.9)-(1.10).

We use the scales (2.12) to write the system (2.4) in non-dimensional form. We rescale the variables u, v, r and z with the scales u_*, v_*, r_* and z_*, respectively. Although we continue to use the same symbols, the variables are, from now on, understood to be dimensionless, except when we compare the model to the experiments. Upon this rescaling, equations (2.4) transform to

$$\begin{aligned} uu_r + wu_z &= -p_r + u_{zz} + \epsilon\Delta_r u \\ \epsilon(uw_r + ww_z) &= -p_z + \epsilon w_{zz} + \epsilon^2\Delta_r' w - g, \end{aligned} \tag{2.16}$$

where $\epsilon = (z_*/r_*)^2 \simeq 0.0003 \ll 1$.

The boundary conditions (2.10)-(2.11) become

$$
\begin{aligned}
p &= 2\epsilon w_z - \epsilon h'(u_z + \epsilon w_r) \\
0 &= 2\epsilon h'(u_r - w_z) - (1 - \epsilon h'^2)(u_z + \epsilon w_r),
\end{aligned}
\tag{2.17}
$$

and the flux conservation (2.9) transforms to

$$
r \int_0^h u \mathrm{d}z = 1. \tag{2.18}
$$

By analogy with (1.15), we drop the terms of order $O(\epsilon)$ and higher in (2.16) and (2.17). The system (2.16) reduces to

$$
\begin{aligned}
uu_r + wu_z &= -p_r + \nu u_{zz} \\
p_z &= -1.
\end{aligned}
\tag{2.19}
$$

The dynamic boundary conditions on the free surface $z = h$ (2.17) become

$$
\begin{aligned}
p &= 0 \\
u_z &= 0.
\end{aligned}
\tag{2.20}
$$

The second equation of (2.19) is easily integrated. Taking into account the no-stress condition (2.20.2) yields the hydrostatic pressure

$$
p(r, z) = h(r) - z, \tag{2.21}
$$

and the first equation of (2.19) transforms to

$$
uu_r + wu_z = -h' + u_{zz}. \tag{2.22}
$$

The approximate momentum equation (2.22) should be solved together with (2.6), (2.18) and the no-stress condition given by (2.20.2). For the system to be correctly posed, one also has to specify the inlet profile at some $r = r_0$: $u(r = r_0, z) = u_0(z)$. For the reader's convenience, we shall collect all the boundary conditions used in the model in one place:

$$
\begin{aligned}
u(r, 0) &= 0 \\
w(r, 0) &= 0 \\
\left.\frac{\partial u}{\partial z}\right|_{z=h(r)} &= 0 \\
r \int_0^{h(r)} u(r, z)\, \mathrm{d}z &= 1.
\end{aligned}
\tag{2.23}
$$

We shall also note that there is a major difference when comparing this problem to the "usual" boundary layer problem. The "usual" boundary layer problem has an inviscid main stream, which the boundary layer flow has to match. Here, no such external flow is present, and instead of matching to the external flow according to (1.18) we have to construct a solution satisfying the boundary conditions for the free surface (2.23.3)-(2.23.4).

2.3 Integral methods

Equations (2.22)-(2.23) encounter the same problems describing the separation of boundary layer within the hydraulic jump as do the classical boundary layer equations (1.19). At the point r_* where the skin friction $u_z(z=0)$ vanishes (separation point), the solutions of (2.22) develop a singularity of the type $u \sim \sqrt{r_* - r}, w \sim 1/\sqrt{r_* - r}$. We have seen that the integral methods of von Kármán and Pohlhausen, described in the previous chapter, can be used in the classical boundary layer theory to describe the separation. Thus, we shall attempt to apply the classical integral methods for flows with a free surface. Again, we use the following idea: although the boundary layer approximations (2.14)-(2.15) break down in a small region around the point of separation, the rest of the flow is described accurately by the boundary layer approximations. If we average the equations in the z direction, the resulting system avoids showing the singular behaviour at the separation, and can adequately describe the flow pattern involving separation of boundary layer.

By integrating (2.22) over z from 0 to $h(r)$ for a fixed r and using the continuity equation (2.6) and the boundary conditions (2.23), we obtain the averaged momentum equation

$$\frac{1}{rh}\frac{d}{dr}\left[r\int_0^h u^2 \mathrm{d}z\right] = -h' - \frac{1}{h}\, u_z|_{z=0}\,. \tag{2.24}$$

We define

$$F_2 = \int_0^h \left(\frac{u}{v}\right)^2 \mathrm{d}z, \tag{2.25}$$

where v is the average velocity

$$v = \frac{1}{h}\int_0^h u(r,z)\mathrm{d}z. \tag{2.26}$$

Conservation of flux (2.23.4) gives

$$vhr = 1. \tag{2.27}$$

Together with (2.27), the integrated momentum equation (2.24) can be written as

$$v(F_2 v)' = -h' - \frac{1}{h}\, u_z|_{z=0}\,. \tag{2.28}$$

The averaged equation (2.28) contains much less information than the full boundary layer equations (2.22). If no assumptions about the profile u are made, then (2.28) is definitely not sufficient for determining the velocity profile. However, if we approximate the velocity u by a certain profile (say, a polynomial profile depending on one parameter, as in von Kármán and Pohlhausen's method described in chapter 1), then (2.28) will specify a differential equation for this parameter and the problem will be well-posed. If we let u depend on N parameters, exactly N integrated equations of the type (2.28) must be specified. Such equations can be obtained by multiplying the momentum equation (2.22) by suitable weight functions, say, u^{n-1}, and integrating with respect to z for $1 \le n \le N$. The weight functions can be arbitrary, the only criterion being that the resulting system of differential equations is non-degenerate. We shall also mention that not all of the equations have to be obtained by integrating the momentum equation (2.28): in the future, we take

(2.22) at $z = 0$, as in the von Kármán and Pohlhausen's method. We have found that using such a "mixture" of integral and non-integral equations does not change the results substantially. However, the equations are algebraically much easier in comparison with the system obtained by pure integral methods.

We shall now commence the derivation of our integral model for the circular hydraulic jump. First, we study models with one parameter $h(r)$ and a fixed (self-similar) velocity profile. As in von Kármán and Pohlhausen's method, the height of the fluid $h(r)$, which for the circular hydraulic jump is the same as the thickness of the boundary layer, will be the only unknown in these self-similar models. We shall show that such models are too simple to describe the structure of the flow inside the jump. Then, we introduce the second parameter $\Lambda(r)$ which will describe the change of the profile. We shall show that such a two-parameter model is sufficient to resolve the flow inside the hydraulic jump.

2.3.1 One parameter model: similarity profile

We remember that in von Kármán and Pohlhausen's model the only unknown function was the thickness of boundary layer, which had to obey equation (1.44). The velocity profile was fixed by the external flow. In the circular hydraulic jump, the height of the fluid $h(r)$ plays the role of the boundary layer thickness. Since there is no external flow, this simplest approximation is to assume a self-similar ansatz for the velocity profile:

$$u(r,z)/v(r) = f(\eta) \tag{2.29}$$

where $\eta = z/h(r)$ and $v(r)$ is the average velocity satisfying (2.27). Equation (2.29) can be rewritten in the alternate form: $w(r,z) = \eta h' u(r,z)$. One can also say that the local inclination of the streamlines at a point (r,z) is proportional to $\eta h' = zh'(r)/h(r)$. Thus, such an ansatz is too simple to describe a flow with separation. However, a lot of information about the flow can be extracted from such a simple model, and this is why we shall briefly describe the results provided by the model. For more details, the reader can consult [6].

Since the velocity profile must satisfy the boundary conditions (2.23) and (2.27), $f(\eta)$ has to satisfy

$$\begin{aligned} &f(0) = 0 \\ &f'(1) = 0 \\ &\textstyle\int_0^1 f(\eta)d\eta = 1. \end{aligned} \tag{2.30}$$

For example, a quadratic profile

$$f(\eta) = 3\eta - \frac{3}{2}\eta^2 \tag{2.31}$$

is the simplest possible polynomial ansatz for the function f, satisfying (2.30). Then, from (2.25), $F_2 = 6/5$ is a constant, and (2.28) becomes

$$\frac{6}{5}vv' = -h' - \frac{3v}{h^2}. \tag{2.32}$$

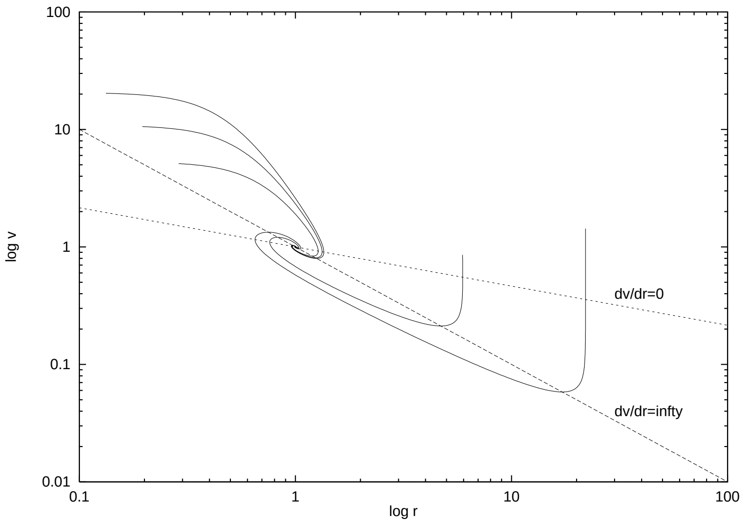

Figure 2.6: Solutions of the model (2.34). The lines $v'(r) = 0$ and $v'(r) = \infty$ are also shown.

Another ansatz for f will still lead to the same form as (2.32) except that the numerical coefficients will be different. There is no qualitative change, however, since all equations of the type (2.32), corresponding to different profile shapes $f(\eta)$, can be further transformed to

$$vv' = -h' - \frac{v}{h^2} \tag{2.33}$$

by suitable rescaling of h, v and r. Equation (2.32) was derived and studied in [1] and [6]. In what follows, we shall call equation (2.33) the Kurihara-Tani equation. With (2.27), the Kurihara-Tani equation (2.33) can be written as an ordinary differential equation for $v(r)$:

$$v'\left(v - \frac{1}{v^2 r}\right) = \frac{1}{vr^2} - v^3 r^2. \tag{2.34}$$

Several solutions of equation (2.34) are shown in figure 2.6. The derivative $v'(r)$ is zero when the right-hand side of (2.34) vanishes, i.e., for $v = r^{-1}$. The derivative $v'(r)$ is infinite if $v = r^{-1/3}$. A solution corresponding to a hydraulic jump should have large velocities for small r and small velocities for large r. However, from figure 2.6 we can observe that such solutions are impossible. All solutions spiral around the point $r = 1$, $v = 1$, which is a stable focus in the (r, v) phase plane. Also, it was proven in [6] that there is no solution for $v(r)$ extending to infinity. Again, one can see from figure 2.6 that at large enough r the velocity suddenly increases, which corresponds to the sharp drop in height, since the height and the velocity are connected through $h = 1/(vr)$. This singularity was interpreted physically in [6] as the end of the plate, where the water runs off. If the radius of the plate is given, we can always find the solution of (2.34), diverging at the end of the plate, which will correspond to the flow after the jump. One can then connect this solution to the solution before the jump by means of a Rayleigh shock, which conserves mass flux (2.1) and momentum flux (2.2). This shock can then be interpreted as the hydraulic jump. The solution before the jump and the position of the shock are uniquely determined [6]. The shock occurs very close to $r = 1$.

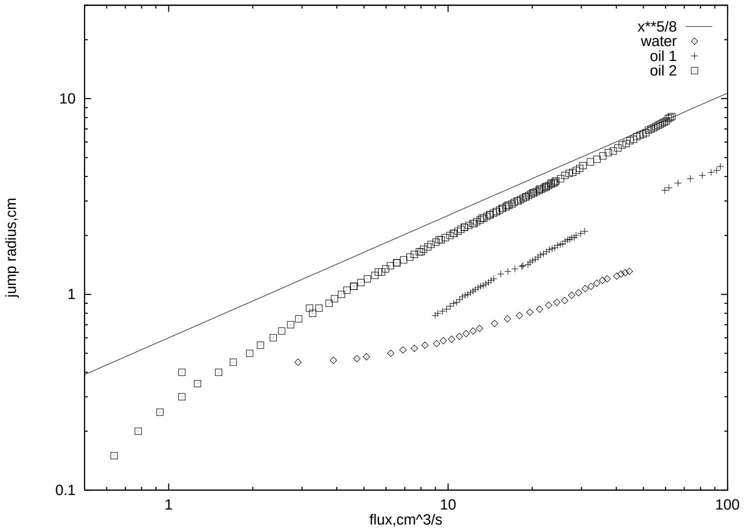

Figure 2.7: The measurements of the radius of the jump versus mass flux for different fluids, courtesy of P. Dimon. The straight line corresponds to $R_j \sim q^{5/8}$.

We remind the reader that all the calculations were performed with dimensionless coordinates. Since the shock occurs very close to $r = 1$ in the dimensionless coordinates, the radius of the jump scales approximately as r_* in the dimensional coordinates from (2.12):

$$R_j \sim q^{5/8}\nu^{-3/8}g^{-1/8}. \tag{2.35}$$

Experiments show a reasonable agreement with the scaling relation (2.35) (see figure 2.7). The radius of the jump indeed scales with the mass flux Q, but the exponent observed in the experiment is larger than $5/8 = 0.625$ suggested by (2.35). Finally, in figure 2.8 we show the height profiles $h(r)$ corresponding to the velocity profiles given in figure 2.6. Even though there is no smooth solution continuing from small r to large r, the shape of the height profile resembles very much the height profiles observed in the experiments (see figure 2.2).

2.3.2 Two-parameter profile

Approximations more sophisticated than (2.29) must be used in order to resolve the flow pattern in the vicinity of the jump and to obtain a solution which smoothly goes through the separation. In order to describe a flow with separation, the function f in (2.29) must be a function of r. An additional "shape parameter" (which we shall call $\Lambda(r)$ to keep our notation consistent with von Kármán and Pohlhausen) must be introduced, and an extra equation for $\Lambda(r)$ must be specified. Here, we generalise ideas developed by von Kármán and Pohlhausen for a boundary layer flow with an external pressure gradient, which is independent it. In our case, the pressure gradient in the momentum equation (2.22) is given by $h'(r)$ since the pressure is hydrostatic (see (2.21)). The physical picture is the following: the change in the velocity profile affects the height, which in turn affects the velocity profile through the hydrostatic pressure (2.21). We shall introduce this coupling between the pressure and the velocity profile by specifying one extra equation for $\Lambda(r)$, which will allow us to describe flows with separation.

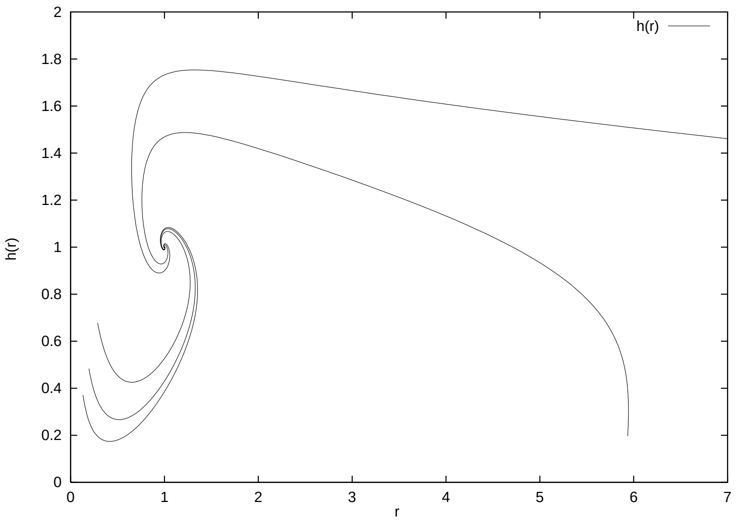

Figure 2.8: The height profiles $h(r) = 1/v(r)$ corresponding to the solutions of the model (2.34).

We approximate the velocity profile by the third order polynomial:

$$u(r, z)/v(r) = a\eta + b\eta^2 + c\eta^3, \tag{2.36}$$

where a, b, c are now functions of r. The boundary condition (2.23) and conservation of flux (2.27) give the following system of equations for the coefficients a, b, c:

$$\begin{aligned} &a + 2b + 3c = 0 \\ &a + b + c = 1. \end{aligned} \tag{2.37}$$

Since (2.37) is a system of 2 equations with 3 unknowns, the coefficients a, b and c can be expressed in terms of one parameter Λ, for example,

$$\begin{aligned} &a = \Lambda + 13/2 \\ &b = -(5/2)\Lambda - 41/4 \\ &c = (4/3)\Lambda + 14/3. \end{aligned} \tag{2.38}$$

The *shape parameter* $\Lambda(r)$ describes the change in the u profile. The separation condition

$$\frac{\partial u}{\partial z} = 0 \tag{2.39}$$

gives $a = 0$, or $\Lambda = -13/2$. The profile is quadratic when $c = 0$, or $\Lambda = -7/2$. Several velocity profiles for different values of Λ are shown in figure 2.9. The velocity profile for $\Lambda = -13/2$ is plotted with a dashed line. If $\Lambda < -13/2$, there is a zone of negative velocity and the flow is separated.

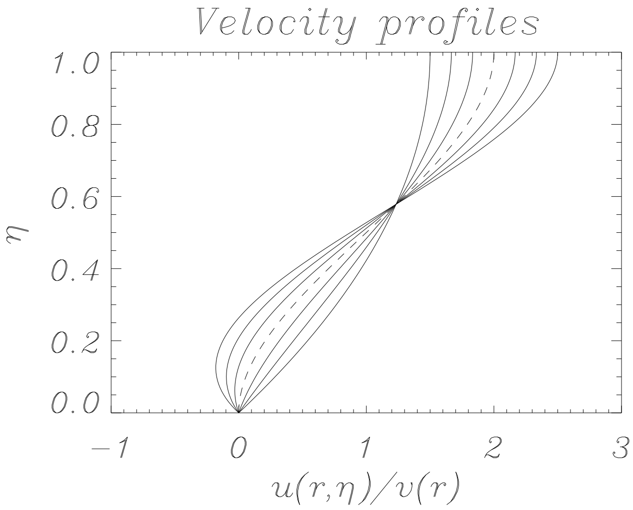

Figure 2.9: Velocity profiles for different values of Λ. The dashed line corresponds to $\Lambda = -13/2$.

Now we have two unknowns $h(r)$ and $\Lambda(r)$ and, correspondingly, we need two equations. The first equation we use is the averaged momentum equation (2.28). Now, however, F_2 is not a constant, but depends on the shape parameter Λ: from (2.25), we have

$$F_2(\Lambda) = 13/12 + \Lambda^2/105. \tag{2.40}$$

We note that there is a certain freedom in choosing the shape parameter Λ, and we have chosen it in such a way that $F_2(\Lambda)$ contains no linear term with respect to Λ.

The second equation, closing the system, is obtained by requiring that (2.22) be satisfied at $z = 0$:

$$h' = u_{zz}|_{z=0}\,. \tag{2.41}$$

An equation of the type (2.41) is also used in von Kármán and Pohlhausen's theory (1.38). However, the *physical* meaning of (1.38) and (2.41) is different, since the pressure in (1.38) is not coupled to the flow inside the boundary layer as it is in our case. Equation (2.41) provides the coupling between the velocity profile and the pressure gradient.

Using (2.40) and (2.38), system (2.28,2.41) can be transformed to

$$\begin{aligned} (F_2(\Lambda)v)' &= (4\Lambda + 14)/h^2 \\ h' &= -v(5\Lambda + 41/2)/h^2. \end{aligned} \tag{2.42}$$

Here, as usual, $v = 1/(rh(r))$ is the average velocity and the prime denotes the derivative with respect to r. Models using more than one shape parameter can be derived in a similar way by specifying additional integrated equations. They tend to be algebraically more complicated than (2.42) without affording any essentially new results.

One can also notice that the boundary layer equations (2.22) require that the derivative u_{yyy} on the bottom vanishes. One therefore expects that better results would be produced by approximating the velocity profile as

$$u = v(r)(a\eta + b\eta^2 + c\eta^4) \tag{2.43}$$

instead of (2.36). We shall note, however, that the system obtained by using the fourth-order profile (2.43) instead of the third-order profile (2.36) is similar to (2.42), but has different values of the numerical coefficients. Such a system does not seem to be more accurate than (2.42) when compared to the experiments. A possible explanation is that both a third-order profile (2.36) and a fourth-order profile (2.43) approximate the true solution only on average with respect to the z variable. In this case, (2.43) does not have any advantages over (2.36). Indeed, a model using (2.43) might be more accurate than (2.42) close to the bottom, but less accurate at the surface.

We shall also note that integral methods are not the only way to describe the separation in the circular hydraulic jump. Another method is to expand the velocity in a power series in z around the point $z = L(r)$, situated somewhere midway between 0 and $h(r)$:

$$u(r,z) = a_0(r) + a_1(r)(z - L(r)) + a_2(r)(z - L(r))^2 + a_3(r)(z - L(r))^3. \tag{2.44}$$

Given the boundary conditions for $u(r, z)$ (2.23.1), (2.23.3) and (2.23.4), we can express all the functions $a_0(r)$, $a_1(r)$, $a_2(r)$, $a_3(r)$ in terms of one parameter (say, $a_0(r)$), as we have done in (2.38). The unknowns in this case will be $h(r)$ and $a_0(r)$. As the first equation, we specify (2.22) at $z = 0$. As the second equation, we take (2.22) at $z = L(r)$. This is the difference with the standard expansion procedure given by (1.35). Collecting terms with different powers of z (or Y in (1.35)) amounts to evaluating the derivatives of (2.22) with respect to z at $z = 0$. If $L(r)$ is chosen in such a way that $u_z(r, z = L(r))$ does not vanish, the resulting system will be able to describe the separation of boundary layer. Moreover, such a system is even capable of describing a roller. The art is to choose $L(r)$ properly. Rather good results are provided by $L(r) = h(r)/2$, but other choices of $L(r)$ are possible.

We shall not pursue this approach because the resulting expressions are so tremendously algebraically complicated that they can only be analyzed using *Mathematica*, and the results for the circular hydraulic jump of type 1 are similar to the ones provided by (2.42). We shall therefore concentrate on the analysis of system (2.42).

2.3.3 Numerical solution of the averaged system

The averaged system (2.42) for h and Λ can be solved as a boundary value problem by specifying two boundary conditions for different values of r. We impose

$$h(r = r_1) = h_1 \text{ and } h(r = r_2) = h_2, \tag{2.45}$$

where the values h_1, h_2 are taken from the experiment and $r_1 < r_2$. Using these two conditions, the function $h(r)$ and the velocity field are determined.

The system is quite sensitive to changes in h when r_1 is chosen to be too small or r_2 is chosen to be too large. Thus, both r_1 and r_2 are chosen to be near 1. A straightforward shooting method from either boundary was enough to obtain a solution. Once a solution of the boundary value problem (2.45) is obtained, it is extended to both $r < r_1$ and $r > r_2$ simply by integrating the system forward from r_2 and backward from r_1.

Figure 2.10 shows the solution from such a boundary value problem, using $h_1 = 1.0$ at $r_1 = 0.8$ and $h_2 = 2.56$ at $r_2 = 1.6$. The two points are taken from the measurement in figure 2.3.

The computed solution $h(r)$ shows a rapid drop at small r, a sharp jump after $r = 0.8$, and a slow decay after the jump. From the plot of $\Lambda(r)$, we observe that the velocity profile changes rapidly near the jump. The separation of the boundary layer ($\Lambda < -13/2$) is

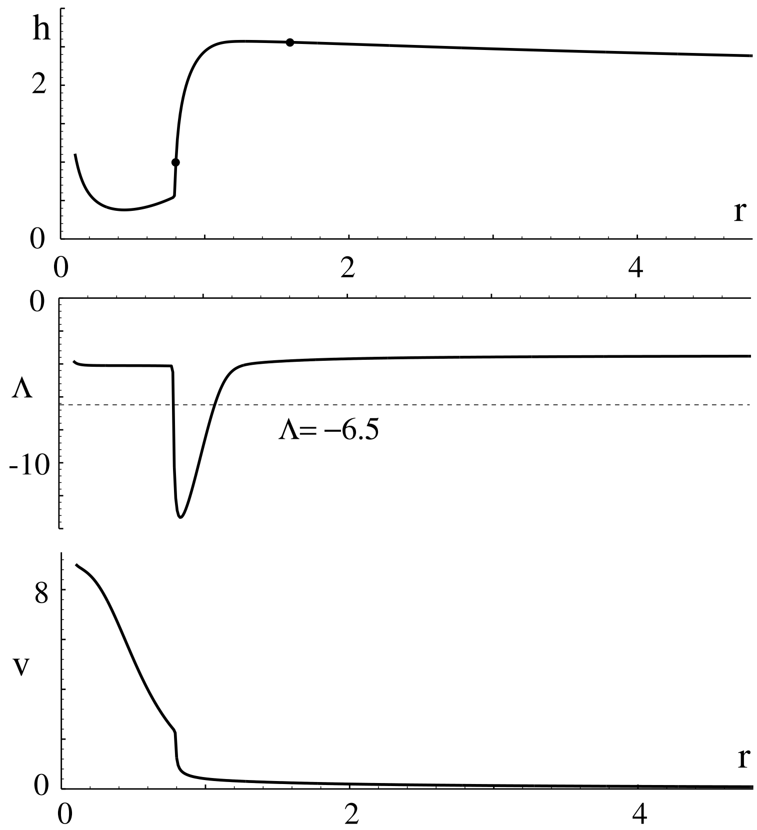

Figure 2.10: Solution of the model (2.42) with h fixed at $r = 0.8$ and $r = 1.6$ (marked with dots in the top picture). The flow is separated when the shape parameter $\Lambda < -6.5$.

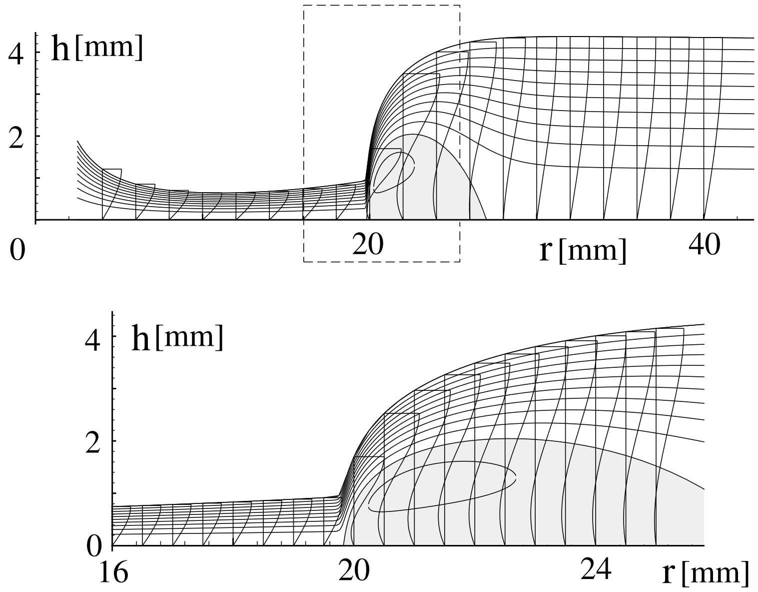

Figure 2.11: Streamlines and scaled velocity u/v profiles for the solution of (2.42) showing a recirculating region (shaded). Note the difference in the scales for the axes. The vicinity of the jump (the dashed box) is enlarged in the lower figure.

observed at the jump. The solution $\Lambda(r)$ appears to converge to $\Lambda = -7/2$ (the quadratic profile) as r becomes large. The average velocity $v = 1/(rh)$ decreases nearly linearly before the jump, and undergoes a rapid decrease at the jump, followed by a slow decay after the jump: $v = 1/(hr) \sim 1/r$, since the height is almost constant for large r.

We shall also plot the solution in terms of a streamfunction ψ, where

$$u = \psi_z/r \quad , \quad w = -\psi_r/r. \tag{2.46}$$

On the bottom $z = 0$ we have $\psi = 0$, and on the surface $\psi = 1$. Inside the separation bubble $\psi < 0$. The contours at $\psi = -0.1, 0, 0.1 \ldots, 1$ are shown in figure 2.11 together with the scaled velocity profile u/v. We have used dimensional units for both axes. The separation bubble extends from $r = 20$ mm to $r = 27$ mm.

Comparisons with the experiments are shown in figure 2.12 and figure 2.13. In figure 2.12 (a), the height profile from the model is compared to the experimental data from [4]. We see that there is a significant deviation in the height profile, and the location of the jump is also off by about 20%. In figure 2.12 (b), the predicted velocity at the surface is compared to the experiment. The almost linear decrease of the velocity before the jump is well reproduced, as well as the sharp drop at the jump. In figure 2.13 the surface velocity in the exterior region is shown. After the jump, the surface velocity is observed to be inversely proportional to r. Thus, we find reasonable agreement between the model and the experiment.

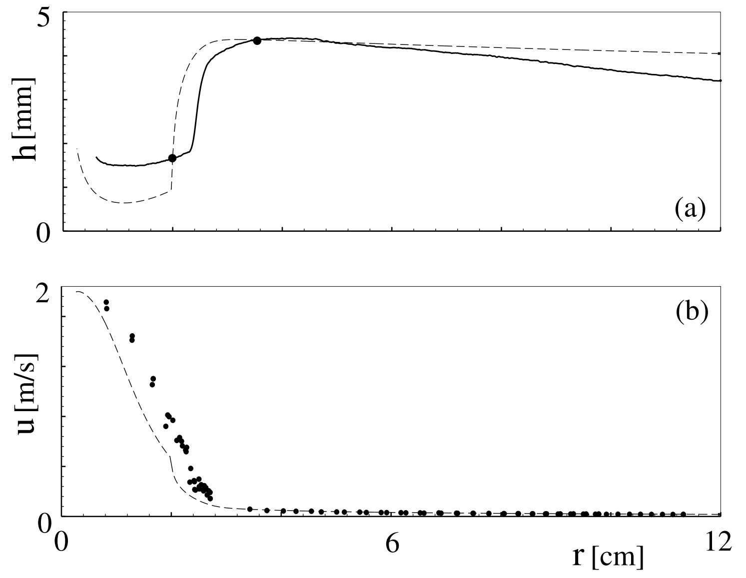

Figure 2.12: Comparison of (a) h and (b) the surface velocity with the experimental data. Solid curve in (a) and dots in (b): experiment [4]. Dashed curves: model. The two dots in (a) show the boundary conditions used in (2.45).

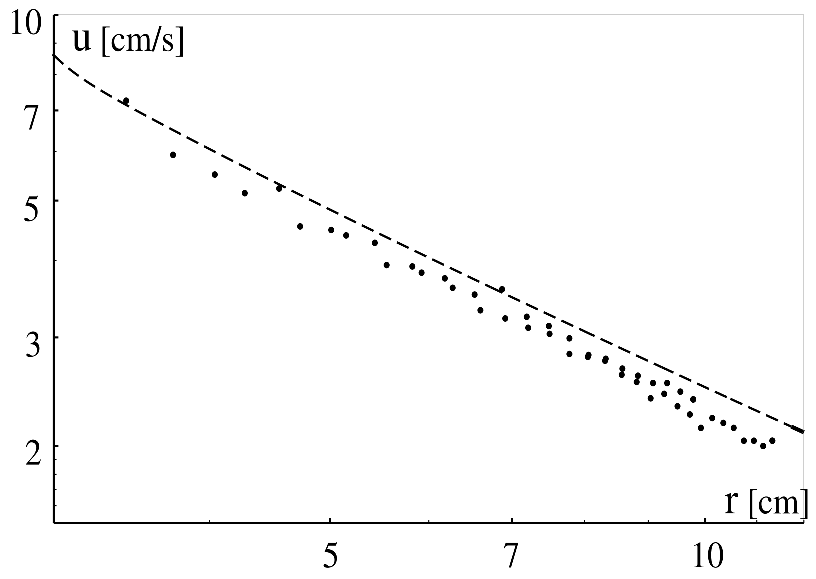

Figure 2.13: The measured velocity in the exterior region [4]. The dashed line shows the model prediction.

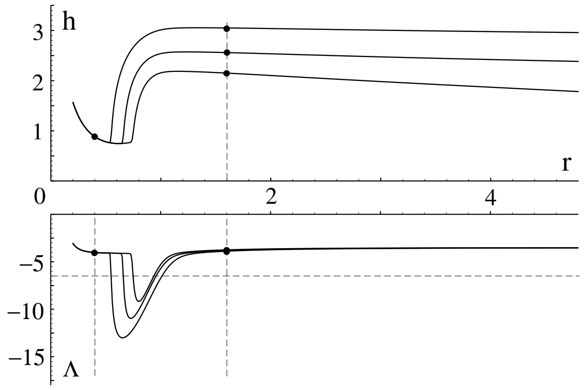

Figure 2.14: Three solutions of (2.45) for the boundary conditions $r_1 = 0.4$, $r_2 = 1.6$, $h_1 = 0.88$, and $h_2 = 2.15$, 2.56, and 3.05.

2.3.4 Increase of the external height. Collapse of the solutions in the interior of the jump

In the experiment, the plate on which the hydraulic jump is formed is submerged in the fluid, and the external height h_{ext} is controlled by moving the plate in the vertical direction. From figure 2.10 we observe that the height is almost constant after the jump, so we can identify the external height with the parameter h_2 in (2.45). By increasing h_2 we can theoretically check how well our model explains the experimental results given in figure 2.3. We choose $r_1 = 0.4$, $r_2 = 1.6$, and $h_1 = 0.88$ and vary h_2 in (2.45).

One can observe from figure 2.3 that even when the external height is increased, the height tends to follow the same profile in the interior of the jump (small r). This experimental feature is well described by our model. In figure 2.14 one can observe that the solutions of (2.45) with different h_2 overlap in the interior of the jump. Of course, these solutions cannot collapse *exactly* onto a single curve because of the uniqueness of trajectories, but the interior parts of the solutions are nearly indistinguishable in the figure. We shall also note that figure 2.14 is obtained by shooting from r_2 and matching at r_1. It is numerically impossible to solve the problem (2.45) by shooting from r_1.

Finally, to compare our model with the experimental data directly, we plot the height profiles from the model and the experiment in figure 2.15. The solutions corresponding to four exterior heights h_2 are shown in figure 2.15 as dashed curves. The corresponding values of Λ from the model are shown in the bottom panel of figure 2.15. As h_2 is increased in the model, the location of the jump moves inward, and the front becomes sharper. We shall also note that, unfortunately, no transition from type 1 to type 2 (see figure 2.4) was observed in the model when h_2 was increased. The solution with a roller is in fact prohibited by the model (2.42). The appearance of a roller at the surface corresponds to the velocity at the surface becoming negative. According to (2.38), the velocity at the surface is

$$U_{top} = v(a+b+c) = v\frac{11-2\Lambda}{6}, \tag{2.47}$$

where $v = 1/(rh) > 0$ is the average velocity. Thus, $U_{top} < 0$ if $\Lambda > 11/2$. However, since we start with $\Lambda < 0$ (and it is easy to see that the point $\Lambda = 0$ is the singular point for (2.42)), a solution to (2.42) cannot reach values with $\Lambda > 0$. Hence, the flow of type 2

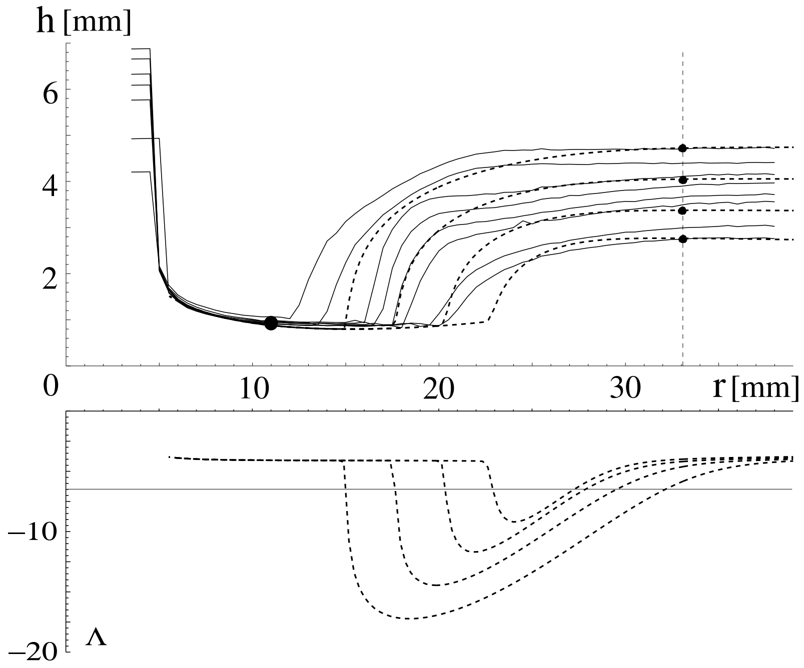

Figure 2.15: (a) Dependence of h on the edge height. Solid: experiment, dashed: model. (b) The shape parameter obtained from the model.

cannot be described by the model (2.42). A possible way of improving the model (2.42) to describe solutions of type 2 is explained at the end of the chapter.

In the following sections, we study the properties of the solutions of (2.42) analytically. Explicit analytic expressions can be derived for the solution before the jump, after the jump and in the region around the jump. Moreover, the analysis of the region around the jump will clarify to what extent the Rayleigh shock conditions (2.1)-(2.2) are satisfied across the jump.

2.4 Asymptotic analysis of the averaged system

2.4.1 Interior

First, we analyse the region before the jump. As we see from figure 2.14, in the inner region, where the collapse of the solutions is observed, the parameter Λ stays close to the value -4.1. From (2.42.2) we observe that when Λ stays close to the value $-41/10$, the height is changing slowly, since $h'(r)$ is small. We thus put $\Lambda(r) = -41/10 + \phi(r)$, where $\phi(r)$ is assumed to be small. We substitute this expression for Λ into the system (2.42), neglecting nonlinear terms in ϕ. In this case, the first equation of (2.42) simplifies to

$$F_2^0 \left(\frac{h'}{h^2 r} + \frac{1}{h r^2} \right) = \frac{2.4}{h^2}, \tag{2.48}$$

where

$$F_2^0 = F_2(\Lambda = -41/10) = (4.1)^2/105 + 13/12 = 1088/875 \simeq 1.243. \tag{2.49}$$

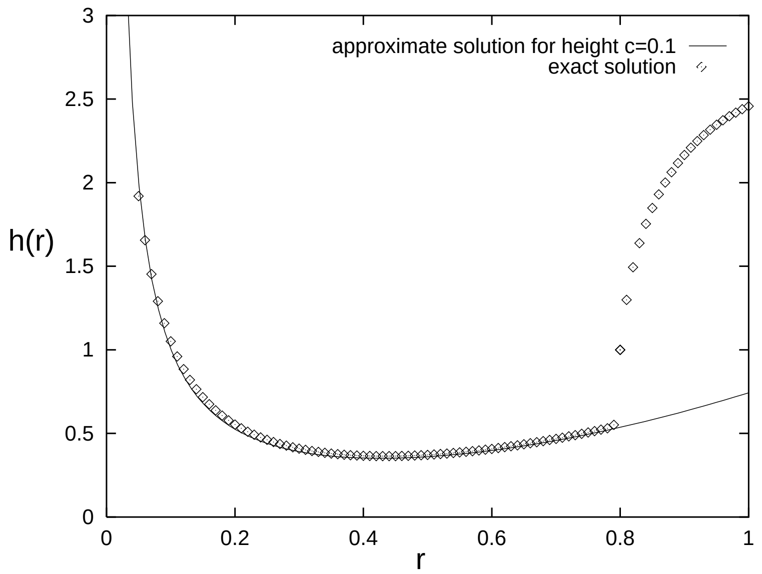

Figure 2.16: Comparison between the numerical solution of equation (2.42) for $h(r)$ (diamonds) compared to (2.51) with $C = 0.1$ (solid line).

Multiplying (2.48) by $h^2 r$, we obtain

$$h' = \frac{2.4}{F_2^0} r - \frac{h}{r}. \tag{2.50}$$

This is a linear equation which can be solved exactly:

$$h = \frac{C}{r} - \frac{0.8}{F_2^0} r^2, \tag{2.51}$$

where C is an arbitrary integration constant.

From the second equation of system (2.42), we get

$$\phi = \frac{r h^3 h'}{5}.$$

Combining this with (2.50) and remembering that $\Lambda = -41/10 + \phi$, we get an expression for Λ:

$$\Lambda = -\frac{41}{10} + \frac{h^4}{5} + \frac{2.4}{5F_2^0} r^2 h^3. \tag{2.52}$$

The agreement between formulas (2.51) and (2.52), and the numerical solution is presented in figure 2.16 and figure 2.17, respectively. The constant C was chosen to be 0.1. We have not tried to perform a numerical fit for the constant C, but rather chose C in such a way that the approximate solution (2.51) is close to the given numerical solution.

Finally, in figure 2.18 we compare the expression (2.51) with the experimental data. The constant C in (2.51) was chosen to be 0.1. The experimental data are plotted in dimensionless coordinates.

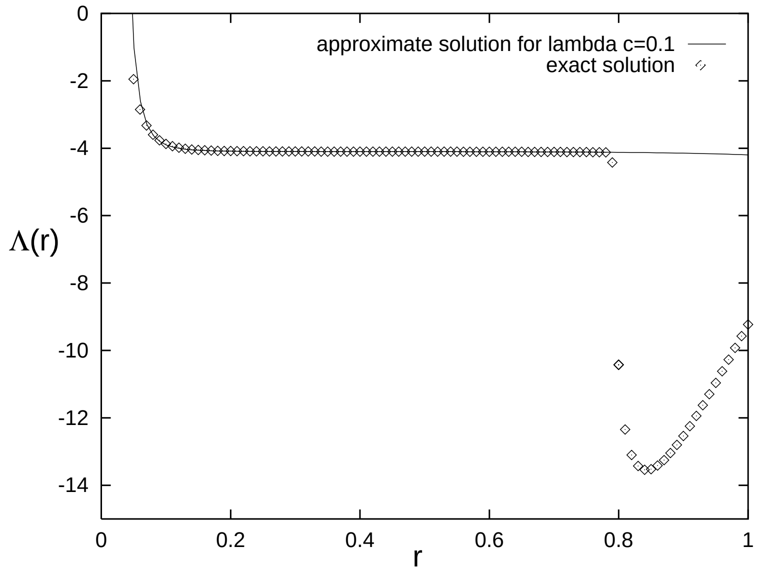

Figure 2.17: Comparison between the numerical solution of equation (2.42) for $\Lambda(r)$ (diamonds) compared to (2.52) (solid line).

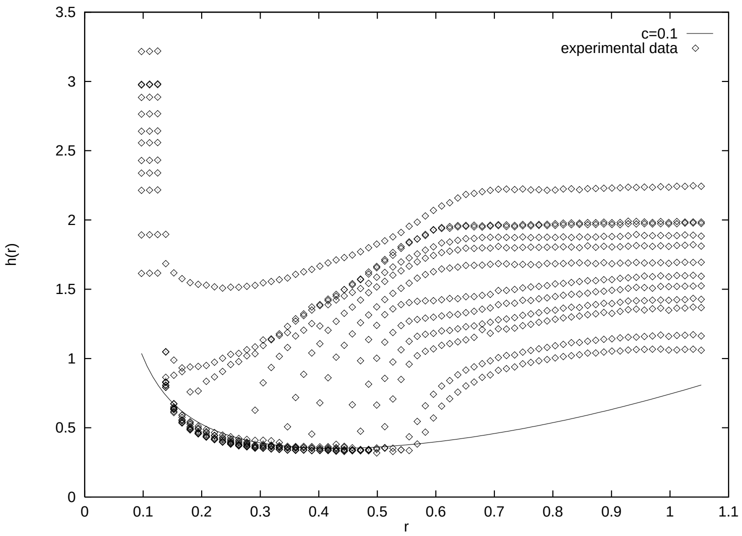

Figure 2.18: Comparison between the asymptotic expression (2.51) (solid line) and the experimental data (diamonds) in the interior of the jump.

2.4.2 Solution after the jump

As we see from the graph of the solution in figure 2.14, Λ tends to the value $-7/2$, which corresponds to a parabolic profile. In this case, the height is given by the second equation of (2.42) with $\Lambda = -7/2$:

$$h' = -\frac{1}{12h^3 r} \tag{2.53}$$

which has the solution

$$h = (C - \log r/12)^{1/4}\,, \tag{2.54}$$

where $C > 0$ is an arbitrary constant. We see that the height goes to 0 at a certain radius $r = r_* = \exp(12C)$. Thus, (2.42), as well as the simpler Kurihara-Tani model (2.32), does not show any regular behaviour when $r \to \infty$. This seems to be a general property of the boundary layer equations: the absence of regular solutions for the system (2.22)-(2.23) when $r \to \infty$ was proved by the author and H. H. Rugh in [9]. We have attributed this lack of asymptotic solutions to the influence of the finite size of the plate. Indeed, a solution with vanishing height such as (2.54) reminds one very much of a flow running off the edge of a circular plate.

Even though the solutions of (2.42) become singular at a finite radius, there is a long 'intermediate' regime $1 \ll r \ll r_*$ where the height is varying very slowly. We intend to prove that the parabolic profile $\Lambda = -7/2$ is stable in this "intermediate asymptotic regime". By stability we mean the stability in the sense of (2.42) and not the stability with respect to time-dependent perturbations of the stationary solution. In other words, we wish to prove that the deviation of Λ from the value $-7/2$ (parabolic profile) will decrease when r increases. We substitute $\Lambda = -7/2 + \phi$ into (2.42) and neglect the nonlinear terms in ϕ. In this case the first equation of (2.42) becomes

$$-\frac{\phi'}{15hr} = \frac{4\phi}{h^2} + \frac{F_2^1}{r^2 h}. \tag{2.55}$$

Here $F_2^1 = (-3.5)^2/105 + 13/12 = 6/5$. Equation (2.55) can be solved exactly:

$$\phi = \exp\left(-\frac{30r^2}{h}\right)\left(C + F_2^1 \int^r \frac{h(r')}{r'} \exp\left(\frac{30r'^2}{h(r')}\right) \mathrm{d}r'\right), \tag{2.56}$$

where C is an integration constant. It is easy to show by the stationary phase method that the solution ϕ in (2.56) for large r behaves as $1/r$. Since ϕ denotes the deviation from the parabolic profile $\Lambda = -7/2$, the parabolic profile is stable in the intermediate asymptotic regime.

2.4.3 Solution around the jump: conservation of momentum

Now we shall consider the region around the hydraulic jump. Recall that in the Kurihara-Tani theory (2.32) the jump was obtained by fitting a shock using conservation of momentum and flux [6]. In this section, we shall show that our theory (2.42) generalises the Kurihara-Tani theory in a natural way.

We introduce a fictitious parameter μ such that the limit $\mu \to 0$ corresponds to the Kurihara-Tani theory and $\mu = 1$ corresponds to (2.42). We rewrite equation (2.42) in the form:

$$\begin{aligned} & V\frac{d}{dr}\{F_2(\Lambda)V\} = -h' - \frac{V}{h^2}(\Lambda + \tfrac{13}{2}) \\ & \mu h' = -\frac{1}{h^3 r}(5\Lambda + \tfrac{41}{2}). \end{aligned} \tag{2.57}$$

Setting $\mu = 0$ gives $\Lambda = -4.1$ from (2.57.2). Then (2.57.1) becomes the Kurihara-Tani equation (2.32), except that the coefficient $6/5$ has to be changed to F_2^0 given by (2.49), since the profile is not parabolic (but still self-similar). A shock is needed to extend the solution from small to large values of r. Suppose the shock is situated at $r = r_0$. Consider a small region of size μ around $r = r_0$. We rescale the independent variable: $r = r_0 + \mu X$. With this rescaling, equation (2.57) becomes

$$\begin{aligned} & \frac{1}{r_0 h}\frac{d}{dX}\{F_2(\Lambda)V\} = -h' + O(\mu) \\ & \frac{d}{dX}h = -\frac{1}{h^3 r_0}(5\Lambda + \tfrac{41}{2}) + O(\mu). \end{aligned} \tag{2.58}$$

From now on in this section, the prime denotes the derivative with respect to X. We see that $\Lambda = -4.1$ is a fixpoint of the system. To match the external solution, we need $\Lambda \to -4.1$ when $X \to \pm\infty$. One might think that this contradicts the requirement that Λ has to tend to $-7/2$ for large r. However, $X \to +\infty$ corresponds to the solutions *immediately after the jump*, and we readily observe from figure 2.14 that immediately after the jump Λ is close to the value -4.1. Convergence to the parabolic profile $\Lambda = -7/2$ is achieved only for much larger r, and this is impossible to capture by our analysis of the 'inner' solution. In other words, convergence of the solution to a parabolic profile is determined by terms of the order μ and higher, which were neglected in (2.58).

Integrating the first equation of (2.58) gives the conservation law:

$$VF_2(\Lambda)/r_0 + h^2/2 = C. \tag{2.59}$$

Physically, the constant C is just the momentum flux density. In fact, the local momentum flux density in the r direction is approximately $u(r,z)^2 + p(z)$ (neglecting terms containing w). Remember also that the pressure is hydrostatic $p(z) = h - z$. Then, averaging the momentum flux density in the z-direction and using the definition of $F_2(\Lambda)$ (2.25) we get precisely (2.59).

Using our expression for Λ from (2.58.2) and substituting it into (2.59), we get an equation for h only:

$$\frac{1}{105}\left(\frac{h'h^3 r_0}{5} + \frac{41}{10}\right)^2 + \frac{13}{12} + \frac{h^3 r_0^2}{2} = Chr_0. \tag{2.60}$$

Suppose that the solution $h(X)$ tends to some constant h_1 when X tends to $-\infty$. Then, the constant C in (2.60) can be expressed in terms of h_1, and (2.60) becomes:

$$\frac{1}{105}\left(\frac{h'h^3 r_0}{5} + \frac{41}{10}\right)^2 h_1 + \frac{13}{12}h_1 + \frac{h^3 r_0^2}{2}h_1 = \frac{1}{105}\left(\frac{41}{10}\right)^2 h + \frac{13}{12}h + \frac{h_1^3 r_0^2}{2}h \tag{2.61}$$

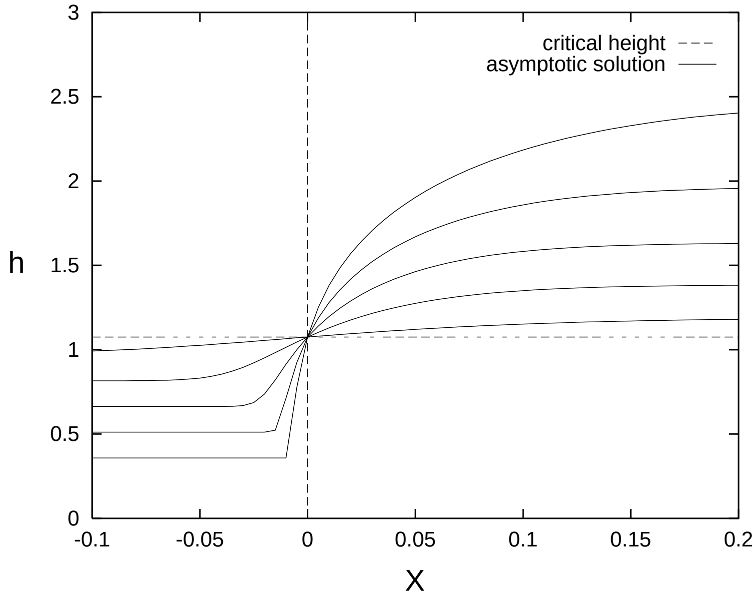

Figure 2.19: Numerical solution of (2.61) with $r_0 = 0.8$ for height as a function of X

The solution of equation (2.61) for different values of h_1 is given in figure 2.19. We have assumed the initial condition $h(X = -\infty) = h_1$ and integrated forward to $X = +\infty$. We see that the solution approaches the final height $h = h_2$ for $X \to +\infty$. When h_1 is close to some critical height H (for given values of parameters H is close to 1), the final height h_2 will be close to H as well, and the the jump amplitude $h_2 - h_1$ becomes very small. This was in fact the criterion for choosing the critical height H, the explicit expression for H will be given immediately below, see (2.64). We also observe that the solution deviates suddenly from $h = h_1$, creating an impression of a sharp corner, and smoothly approaches $h = h_2$. When the amplitude of the jump tends to 0, the solution $h(X)$ becomes increasingly smooth.

We make a comparison between the full numerical solution of (2.42) and the solution of (2.61). In figure 2.20 and figure 2.21 we compare the solutions for h and Λ, respectively. We see that the model based on local momentum conservation (2.59) works quite well. The agreement is even more surprising considering that local conservation of momentum flux for the jump (2.59) has been obtained in the limit $\mu \to 0$. However, $\mu = 1$ and there is no reason to expect that conservation of momentum will be so accurate.

The result of this section will be devoted to the detailed analysis of (2.61) and might seem a little technical. We shall explain why the solution deviates from $h = h_1$ so sharply and approaches $h = h_2$ smoothly and derive an analytic expression for the solution of (2.61) when the amplitude of the jump $h_2 - h_1$ is very small. We present this analysis for the sake of completeness. A reader who does not find such a detailed analysis interesting can skip the rest of this section and go directly to the last section of this chapter.

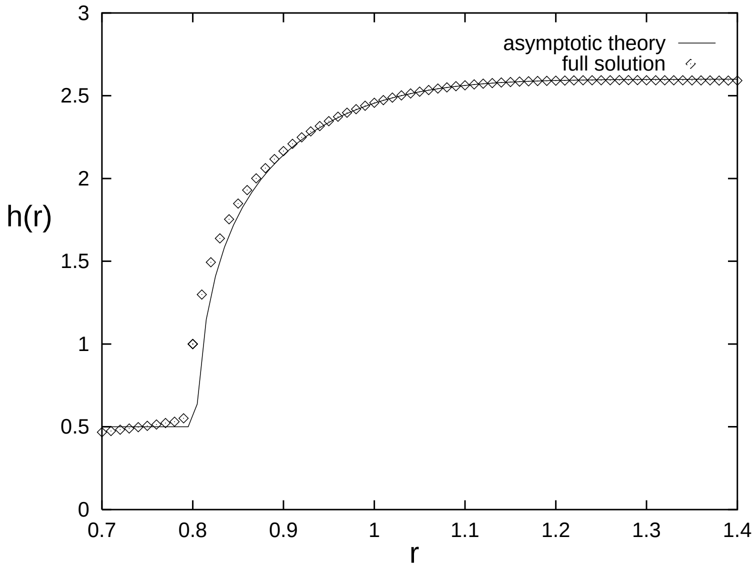

Figure 2.20: Comparison between the full numerical solution of (2.42) (diamonds) and the approximate equation (2.61) (solid lines) for h.

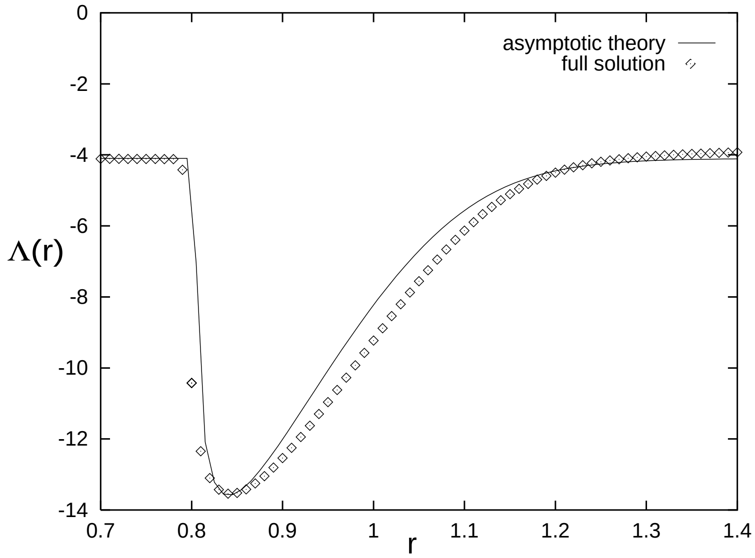

Figure 2.21: Comparison between the full numerical solution of (2.42) (diamonds) and the approximate equation (2.61) (solid lines) for Λ.

Fixpoints $h = h_1$ and $h = h_2$ and the expression for the critical height

Equation (2.61) has two fixpoints: $h = h_1$ and $h = h_2$, which are connected by the conservation law (2.59) with $\Lambda = \Lambda_0 = -4.1$. We write, as before,

$$F_2^0 = F_2(\Lambda = -4.1) = \frac{(-4.1)^2}{105} + \frac{13}{12} \simeq 1.243.$$

Then, conservation of momentum flux (2.59) gives

$$\frac{2F_2^0}{h_1 r_0} + h_1^2 r_0 = \frac{2F_2^0}{h_2 r_0} + h_2^2 r_0,$$

which can be transformed to

$$(h_2 - h_1)(2F_2^0/r_0^2 - h_1 h_2 (h_1 + h_2)) = 0. \tag{2.62}$$

Given h_1, the final height h_2 can be found from (2.62). One (trivial) solution is $h_2 = h_1$, while another is

$$h_2 = \frac{h_1}{2}\left(-1 + \sqrt{1 + \frac{8F_2^0}{r_0^2 h_1^3}}\right). \tag{2.63}$$

(The solution with the minus sign corresponds to $h_2 < 0$ and has to be discarded as unphysical). We assume that $h_2 \geq h_1$. When the initial height h_1 tends to the critical height H, the height of the jump $h_2 - h_1$ must tend to zero.

With the help of (2.63), it is easy to write down the expression for the critical height H. Putting $h_1 = h_2 = H$ in (2.62), we obtain

$$H = \left(\frac{F_2^0}{r_0^2}\right)^{1/3}. \tag{2.64}$$

The stability of the fixpoints h_1 and h_2 with respect to (2.61) can be computed analytically. Linearising (2.61) around the point h_i (where $i = 1, 2$), we get $\delta h_i' = K_i \delta h_i$, where

$$K_i = \frac{3264}{41}\frac{H^3 - h_i^3}{r_0 h_i^4} \tag{2.65}$$

and the prime denotes the derivative with respect to X. We have assumed that $h_1 < H$ and $h_2 > H$. In this case, $K_1 > 0$ and $K_2 < 0$, thus the fixpoint $h = h_1$ is unstable and $h = h_2$ stable. We also note that since h_1 is generally small, the transition away from the unstable fixpoint h_1 happens very quickly, thus giving an impression of a "sharp corner" in the lower part before the jump (see figure 2.19). On the other hand, if h_2 is large, the absolute value of K_2 will be small, thus the curve close to $h = h_2$ will be much smoother. As h_1 (and h_2) tends to H given by (2.64), the stability coefficients K_1 and K_2 both tend to zero, thus making the solution $h(x)$ smoother.

Limit of small jump $h_2 - h_1 \to 0$

When the height difference $h_1 - h_2$ is small, an analytic formula for the solution can be written down. In this case, the solution $h(x)$ will be close to H and h' will be small. If terms of the order h'^2 are neglected, we can rewrite (2.61) as

$$\frac{82}{10875}\frac{h' h^3}{r_0} h_1 = r_0^2 (h - h_1)(h_2 - h)(h + h_1 + h_2). \tag{2.66}$$

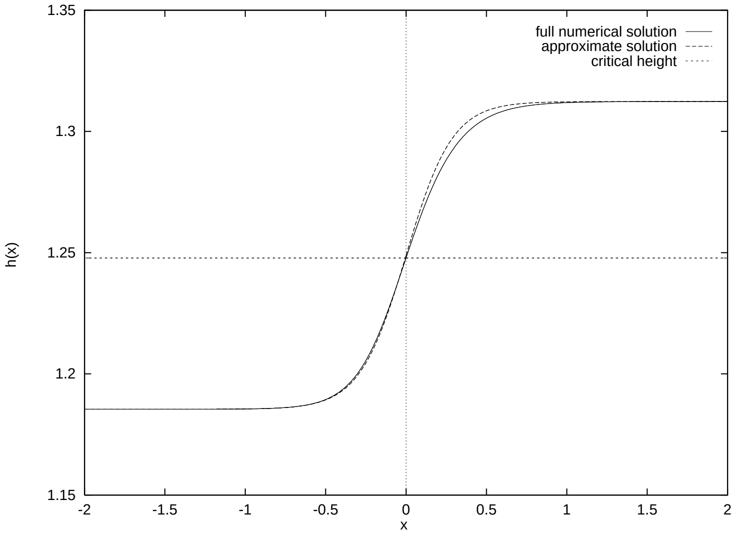

Figure 2.22: Comparison between the full numerical solution of (2.61) and the small jump limit (2.68).

Setting $h + h_1 + h_2 \simeq 3H$, $h^3 \simeq H^3$, we get

$$h' = \frac{10875}{82} \frac{r_0}{H^3} (h - h_1)(h_2 - h). \tag{2.67}$$

Consequently, in the small jump limit $h_1 \to H$, the solution of (2.61) is given by

$$h(x) = \frac{h_1 + e^{Mx} h_2}{1 + e^{Mx}}. \tag{2.68}$$

The expression for the constant M in (2.68) is

$$M = \frac{10875}{82} \frac{r_0(h_2 - h_1)}{H^3}. \tag{2.69}$$

One can check that (2.69) is consistent with (2.65) in the limit $h_2 \to H$.

In figure 2.22, we illustrate the accuracy of our analysis by comparing the numerical solution of (2.61) and (2.68) for $r_0 = 0.8$ and $h_1 = 0.95H$. The agreement between the approximate solution (2.68) and the exact numerical solution of (2.61) is quite good.

2.5 Possible ways of predicting the wave-breaking bifurcation

In this section, we shall develop an idea which might lead to a prediction of the wave-breaking bifurcation. We shall emphasise that the model described below is very preliminary and can hardly be considered a success. The model tries to include some terms neglected in the boundary condition (2.17) due to the boundary layer approximation.

We shall remind the reader that the wave-breaking bifurcation in the hydraulic jump manifests itself in two ways:

1. The height profile $h(r)$ becomes smoother in the neighbourhood of the jump,

2. A recirculating region (roller) appears on the top of the jump. There is still a separation bubble on the bottom. The roller is located inside the separation bubble, as is illustrated in figure 2.4(b).

It is natural to think that at the wave-breaking bifurcation solutions of both type 1 and type 2 exist, but that one of them becomes unstable. This instability is impossible to predict from the time-independent models. However, it would be desirable if the time-independent model gave two distinct types of solutions. Then, the stability analysis around these time-independent solutions could be performed, and the bifurcation would show up as one of the solutions becoming unstable.

We are quite convinced that the model (2.42) does not yield two distinct types of solutions. At least, the velocity at the surface for a solution of (2.42) cannot become negative. Indeed, the velocity at the solution becomes negative when $\Lambda > 11/2$, and since $\Lambda = 0$ is a singularity, and we start with the values $\Lambda < 0$, this type of solution is forbidden. One can think of many reasons why the model (2.42) fails to describe a state with a roller. For example, we have used the boundary condition at the surface

$$\frac{\partial u}{\partial z}|_{z=h} = 0 \ . \tag{2.70}$$

However, the exact boundary condition, describing the vanishing tangential stress at the surface, is given by the second equation of (2.17). We can approximate this exact condition (2.17.2) with an accuracy $O(\epsilon h'^2)$ as

$$\left.\frac{\partial u}{\partial z}\right|_{z=h} = 2\epsilon h' \frac{dU_s}{dr} \ . \tag{2.71}$$

Here $U_s = u(r, z = h(r))$ is the surface velocity.

We can try to develop a model analogous to (2.42) using the modified boundary condition (2.71) instead of (2.70). In this section we shall approximate the velocity profile by the polynomial ansatz (2.43). The models which use (2.43) and (2.36) show qualitatively the same behaviour, but there is a quantitative difference in their coefficients. We have found that (2.43) gives results which compare better to the experiments and therefore we will use this ansatz for the remaining part of this chapter. The reader can easily generalise the results for the profile (2.36).

The coefficients a, b, c have to satisfy the flux conservation condition,

$$a/2 + b/3 + c/5 = 1. \tag{2.72}$$

Since (2.71) is no longer an algebraic equation in the coefficients, we cannot express all the variables a, b and c in terms of one parameter Λ as we did in the derivation of (2.42). We thus get a model with *two shape parameters* a and b. Since $h(r)$ is also unknown, we have three unknowns: $a(r)$, $b(r)$ and $h(r)$, which require three equations for the system to be properly defined. We choose (2.71) as the first equation. Following the derivation of (2.42), we choose the average momentum equation (2.28) as the second and the momentum equation (2.22), evaluated at $z = 0$, as the third equation. We obtain the following system

$$\begin{aligned} &2\epsilon h' \frac{d}{dr}\left\{v(a+b+c)\right\} = \tfrac{v}{h}(a+2b+3c) \\ &\frac{d}{dr}\left\{vF_2(a,b)\right\} = \frac{3v}{h^2}c \\ &h' = \frac{2v}{h^2}b, \end{aligned} \tag{2.73}$$

where $c = 5(1 - a/2 - b/3)$ from (2.72). The function $F_2(a, b)$ is

$$F_2(a,b) = \int_0^1 \left(\frac{u}{v}\right) \mathrm{d}\eta = \frac{25}{11} - \frac{65a}{77} + \frac{173a^2}{924} - \frac{35b}{132} + \frac{289ab}{1848} + \frac{71b^2}{1980}. \tag{2.74}$$

When $h' = 0$, the first equation of (2.73) becomes the algebraic condition $a + 2b + 3c = 0$. Thus, the order of the system (2.73) suddenly drops from 3 to 2. This is manifested in the appearance of a singularity in the solutions of (2.73) when $b = 0$. Computing the derivatives a' and b' from (2.73), we get

$$\begin{aligned} a' &= \frac{G_a(a,b,h,r)}{bD(a,b)} \\ b' &= \frac{G_b(a,b,h,r)}{bD(a,b)} \\ h' &= \frac{2v}{h^2}b, \end{aligned} \tag{2.75}$$

where the functions G_a, G_b and D are polynomials in a and b, whose exact form is too complicated to be useful. We shall not present them here since the particular form of these functions is of no interest to us. We have used the symbolic calculation package *Mathematica* to derive and analyse (2.75).

The singularity $b = 0$ in (2.75) corresponds to $h(r)$ reaching extremum $h' = 0$. *Physically*, however, there should be no singularity at $h' = 0$, since at this point the boundary layer approximation is best justified. Therefore, it is reasonable to require that the solution of (2.75) remains non-singular when $b = 0$. This is possible if at the point r_* where $b(r)$ vanishes, both $G_a(a, b, h, r)$ and $G_b(a, b, h, r)$ vanish also. Then, both the numerator and denominator in the expressions (2.75) for a' and b' vanish, and a smooth solution passing through the singular point $b = 0$ is possible. Using *Mathematica*, we see that both $G_a(a, b, h, r)$ and $G_b(a, b, h, r)$ vanish at the point r_* where $b(r_*) = 0$ if $a(r_*) = 30/13$. From (2.72), the coefficient $c(r_*)$ at this point has the value $c(r_*) = -10/13$. Thus, at the point r_*, corresponding to the extremum of the height $h'(r_*) = 0$, the velocity profile has to take the following form:

$$u(r,\eta) = v(r)\left(\frac{30}{13}\eta - \frac{10}{13}\eta^4\right). \tag{2.76}$$

We have used this method to compute the non-singular solutions of (2.73). Several such solutions are shown in figure 2.23. Depending on the position of the height extrema, the solutions either exhibited a sharp increase in height $h(r)$ (marked 'type 1' in the figure) or a slow raise (marked 'type 2') when r was increased. The problem of describing the wave-breaking would have been solved if the solutions marked 'type 2' on figure 2.23 reached a negative velocity on the surface of the fluid, and the solutions of 'type 1' did not have this property. Unfortunately, this is not the case for our model. All the solutions shown in figure 2.23 have a positive surface velocity. This time, it is possible for a solution of (2.73) to reach a negative surface velocity in some cases. However, there is no definite rule that only 'smooth' solutions of 'type 2' in figure 2.23 exhibit such a wave-breaking, whereas the top velocity for the solution of 'type 1' remains positive. If the height of the maximum is large enough, both solutions of 'type 1' and 'type 2' can have a region in r where the surface velocity is negative.

One can also criticise the following aspects of the model (2.73):

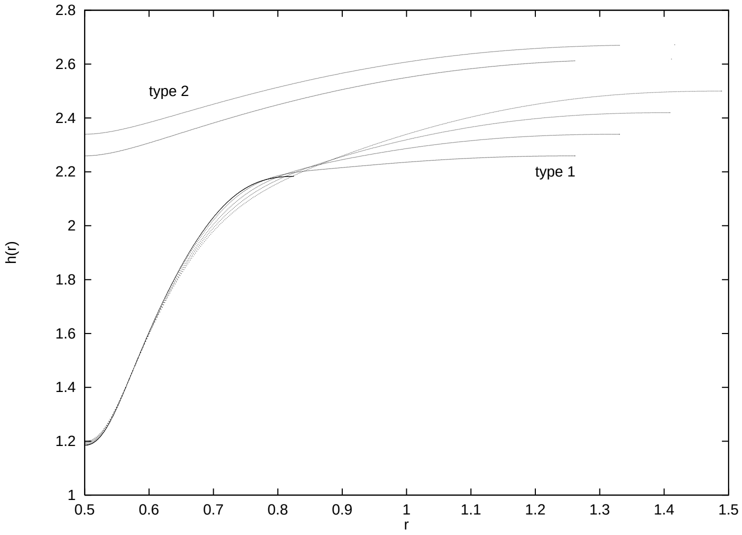

Figure 2.23: Different types of height profiles $h(r)$ given by the system (2.73).

1. The velocity profile at the extrema of height is fixed by (2.76). This condition is very restrictive. Consider, for example, the region of rising height in the inner part of the jump. The condition (2.76) requires that the separation eddy and the roller (if the latter is observed) must occur in between the values of r corresponding to the minimum and the maximum of height, i.e., on the inner side of the jump. This is in contradiction with the observations. Both the separation eddy and a roller in the experiments seem to end at a radius much larger than where the height has reached its maximum.

2. The numerical solution of the system (2.73) is much more difficult than the solution of (2.42). One has to find a heteroclinic orbit connecting the points $a = 30/13, b = 0, h = h_0, r = r_0$ (minimum in height) to the point $a = 30/13, b = 0, h = h_1, r = r_1$ (maximum in height) by fixing the parameters h_0 and h_1, say, which has to be done with quite sophisticated algorithms.

In view of the criticism presented above, we shall consider the model (2.73) as a half-failure. However, we still think that the results presented in figure 2.23 are encouraging. Also, this model has taught us a way to deal with the singularities which appear when the boundary conditions are improved to include non-boundary layer effects. Therefore, we hope that this section will be a stepping stone to a better model which can explain the wave-breaking bifurcation.

2.6 Conclusion

In this chapter, we have developed a theory for the circular hydraulic jump. The model allows us to capture several experimental features which were not possible to explain before. Moreover, we have constructed analytic expressions for different parts of the solution and retrieved the conservation of momentum, proposed by Lord Rayleigh. There are several interesting experimental features, a successful theoretical explanation of which has so far eluded us. The first one is the transition from a type 1 to type 2 hydraulic jump (the wave-breaking bifurcation). The second problem is the breaking of the radial symmetry and the formation of polygons shown in figure 2.5. We hope that these phenomena can be explained in the future by further development of the integral method approach described in the chapter.

Bibliography

[1] Tani, I. (1949) *J. Phys. Soc. Japan* **4**, 212.

[2] Craik, A.D.D., Latham, R.C., Fawkes, M.J. & Gribbon, P.W F. (1981) *J. Fluid Mech.* **112**, 347.
Ishigai, S., Nakanishi, S., Mizuno, M. & Imamura, T. (1977) *Bull. J.S.M.E* **20**, 85.
Nakoryakov, V.E., Pokusaev, B.G. & Troyan, E.N. (1978) *Int. J. Heat Mass Transfer* **21**, 1175.
Olsson, R.G. & Turkdogan, E.T. (1966) *Nature*, **211**, 813.

[3] Kurihara, A. (1946) *Rep. Research Institute for Fluid Engng, Kyusyu Imperial University* **3**, 11.

[4] Ellegaard, C., Hansen, A. E., Haaning, A. & Bohr, T. (1996) *Physica Scripta* **T67**, 105.
Ellegaard, C., Hansen, A. E., Haaning, A. & Bohr, T. (1996) *Physica B*, **228**, 1.
Bohr, T., Ellegaard, C., Hansen, A. E., Hansen, K., Haaning, A., Putkaradze, V. & Watanabe, S. *Physica A*, submitted.

[5] Watson, E.J. (1964) *J. Fluid Mech.* **20**, 481.

[6] Bohr, T., Dimon, P. & Putkaradze, V. *Shallow-water approach to the circular hydraulic jump, J. Fluid Mech.* **254**, 635.

[7] Whitham, G.B. (1974) *Linear and Nonlinear Waves*, Wiley-Interscience.

[8] Landau, L. D. & Lifshitz, E. M. (1987) *Fluid Mechanics*, Pergamon.

[9] Putkaradze, V. & Rugh, H. H., *Non-Analyticity of the Boundary Layer Flows with a Free Surface*, preprint.